Multipath Measurements at the Lunar South Pole from Opportunistic Ground-based Observations — Part I: Experiment Concept

Marc Sanchez Net,* Nereida Rodriguez-Alvarez,* Daniel Kahan,* David D. Morabito,* and Harvey M. Elliott†

ABSTRACT. — This article describes an experimental campaign to measure multipath effects between the Lunar Reconnaissance Orbiter (LRO) and the Deep Space Network (DSN) when the spacecraft sets behind or rises from the far side of the Moon. The primary objective of this campaign was to measure the Doppler spread of the received reflections and characterize the extent of the scattering area from terrain properties such as surface roughness. All experiments were conducted opportunistically without imposing any operational constraints or requirements to LRO. This approach expedited the measurement campaign, but also limited the resulting science output.

In this article, we describe the experimental setup and provide an exploratory analysis of the collected samples. In particular, we first describe the experiment planning phase, including coordination with the LRO project, selection of DSN tracks, and information on the sequence of events that occur during each measurement opportunity. Next, we analyze three of the nine DSN tracks executed. This exploratory analysis includes measurements of the received signal-to-noise ratio (SNR) and residual frequency, as well as estimation of the specular reflection point and its associated Doppler shift. Finally, a discussion on how the available data can be used to estimate the scattering area.

This article is intended as an introduction to this effort. A companion article provides an in-depth discussion of the science results, including estimation of the Doppler spread and the scattering area.

---

*Communications Architectures and Research Section.

†Flight Communications Systems Section.

The research described in this publication was carried out by the Jet Propulsion Laboratory, California Institute of Technology, under a contract with the National Aeronautics and Space Administration.

I. Introduction

A. Motivation

The lunar south pole has been an area of renewed scientific and programmatic interest over the last few years. From a scientific perspective, the possibility that water ice could be present in permanently shadowed regions has been an ongoing debate for several decades. In 1994, the Clementine spacecraft conducted a set of bistatic radar measurements with the DSN and reported an enhancement of the cross-polarization ratio (CPR) at low bistatic angles when the reflection was focused over non-illuminated areas of the lunar south pole [1]. Similar enhancements were not observed in sunlit areas, leading to the conclusion that water ice was present. Later work has, however, disputed these conclusions and argued that changes in CPR are linked to changes in surface roughness, not water ice [2, 3].

From a programmatic perspective, NASA's Artemis program is currently seeking to place astronauts at the south pole of the Moon by 2024 [4]. This site, while interesting from a science-return point of view, poses challenges for direct communication with Earth. The geometry of the Earth-Moon system dictates that landed assets view Earth at very low elevation angles (typically less than 6°), thus making the link back to Earth susceptible to multipath fading effects [5]. These effects, in turn, cause the received signal at a DSN station to experience large variations in received power[1], which degrade link performance and ultimately pose safety concerns that need to be addressed and mitigated prior to launching Artemis.

Given that measurements of reflections from the lunar south pole can lead to both scientific and programmatic advances, this paper describes an opportunistic campaign conducted during the first half of 2020 between the Lunar Reconnaissance Orbiter and the DSN. This campaign was opportunistic in that no changes to LRO or its ground stations were needed.

B. Research Objectives

The measurement campaign is motivated by three primary objectives:

1. Programmatic objective: Measure the Doppler spread of the received signals and compare it to analytic predictions from a previous article [5].
2. Scientific objective: Study surface roughness signatures observed in both the Doppler spread and CPR of the reflected signal from the lunar south pole.
3. Programmatic and scientific objective: Measure the relative permittivity of the lunar south pole from the scattered signal.

---

[1]The Volatiles Investigating Polar Exploration Rover, or VIPER, a rover expected to land on the lunar south pole as early as December 2022, is budgeting 16 dB of power margin to mitigate deep fades caused by multipath reflections [6].

This paper serves as an introduction to the measurement campaign. As such, we mainly focus on the experimental setup and a qualitative analysis that demonstrates our ability to measure scattered signals from the lunar south pole. Additional analyses with the recorded samples are expected to be published in future issues of this journal.

The rest of this article is organized as follows. Section II starts with a discussion of the experiment concept, including its geometry, transmitting and receiving antennas, and coordination with the LRO project. We also detail how DSN tracks were selected and specify the configuration of the DSN open-loop receivers (OLRs). Section III provides an initial analysis of the collected measurements, including received SNR, Doppler residuals, scattering signatures, and determination of the scattering area using iso-delay and iso-Doppler curves. Finally, we conclude the paper with a summary of work performed to date and opportunities for further research.

II. Experimental Setup

A. Concept

Our experiment is conceptually simple: use an OLR to capture discrete samples of the in-phase and quadrature components of LRO's S-band (2271.2 MHz) downlink signal as the spacecraft sets and rises from the far side of the Moon. LRO is currently in a near-polar low altitude orbit with an approximately 2-hour period. Therefore, the spacecraft overflies the lunar south pole with this same cadence giving us numerous opportunities to record scattered signals from that part of the Moon.

The system geometry is heavily constrained by the opportunistic nature of this measurement campaign. For instance, LRO's transmitter is turned on approximately 3 minutes before acquisition of signal (AOS) from its primary ground station, located at White Sands, NM, and turned off 5 minutes after loss of signal (LOS). Both AOS and LOS are routinely scheduled so that they occur when surface grazing events are no longer a concern, and could not be modified for the purposes of this experiment. Therefore, it is unlikely that the main beam of LRO's high-gain antenna (HGA) ever illuminates the Moon's surface while the radio is turned on and, consequently, we will at best measure reflections from the HGA's secondary lobes.

On the other hand, LRO's operations team commands the spacecraft's HGA to always maintain Earth pointing (even while flying over the far side of the Moon). This facilitates the experiment since White Sands and Goldstone, one of three DSN complexes, are close enough in latitude and longitude that they both fall within the -3 dB beamwidth of LRO's HGA. Therefore, having LRO point to White Sands is sufficient for us to shadow its downlinks silently and acquire the desired samples.

The combination of all these factors results in a system geometry that limits our ability to perform measurements at a wide variety of bistatic and incidence angles. Indeed, all measurements collected will have very large incidence and bistatic angles (close to

$\theta \approx 90^\circ$ and $\phi \approx 180^\circ$, respectively) regardless of whether the grazing event occurs while LRO sets or rises. To exemplify this limitation, Figure 1 provides a schematic view of the system geometry in two dimensions. The orange arrows represent the rays departing from the spacecraft, illuminating the surface of the Moon, and arriving at the DSN station. Note that in reality, the DSN station is located on the northern hemisphere, a consideration that has been obviated for clarity.

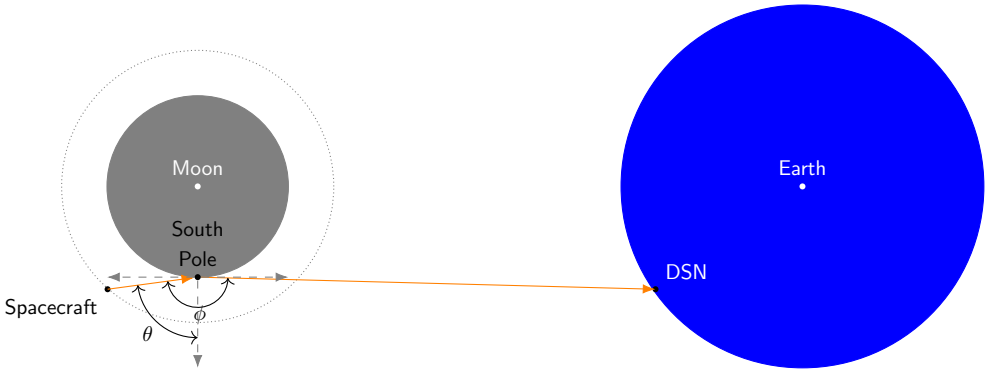

Figure 1. System Geometry (Distances not to Scale)

B. Coordination with the LRO Project

Coordination between several entities was required to conduct the proposed experiment. Initially, we focused our efforts on understanding if surface grazing events could be captured without any changes to LRO operations. This included, for instance, gathering information on LRO's telecommunications subsystem, operational schedule, as well as configuration parameters, such as antenna pointing and transmitter on and off times. We also considered whether our experiment could be performed using standard data products provided by the operational closed-loop receivers at White Sands. Unfortunately, these receivers produce measurements at second-level resolution, which was deemed insufficient for our purposes. Therefore, we decided to use a DSN station configured in open-loop receive mode to shadow scheduled White Sands tracks.

Since the DSN occasionally supports LRO at S-band, assigned personnel, including the Network Operations Engineer (NOPE) and Mission Interface Manager (MIM), were available to request DSN support for this spacecraft. Both the NOPE and MIM coordinated each shadowed track with the LRO project to ensure that we were not imposing any operational constraints on the mission, and that we were made aware of any changes to the spacecraft's operational schedule. We also directly coordinated with LRO personnel at White Sands Operations Center and Goddard Space Flight Center (GSFC).

Once the desired DSN tracks were identified, we interfaced directly with the DSN Scheduling Office to allocate DSN antenna time to coincide with periods before White Sands AOS and/or after LOS. In cases of successive orbits where the time period between tracks was too short, we requested that the activity be allocated as one track (if

there were no conflicts). In addition, the equipment that was usually included for each track included standard DSN tracking at S-band. The open-loop receiver allocation, however, was handled independently by the Radio Science Support Team, which eliminated the need to directly schedule time on the operational DSN open-loop receivers.

Finally, after each shadow track was executed, we requested reconstructed trajectories and orientation kernels from the LRO operations team and the Flight Dynamics Facility (FDF). The trajectories were used in conjunction with specialized software to analyze the multipath event and generate the results discussed in Section III.

C. Selection of Tracks

The measurement campaign was conducted over a 6-month period. Given that LRO overflies the south pole approximately every 2 hours, hundreds of candidate experiment opportunities were initially available, one for each track scheduled between LRO and White Sands. Three criteria were used to down-select opportunities:

- The grazing event should occur while LRO's HGA main beam illuminates the surface of the Moon (as opposed to the side-lobes). These illumination conditions enhance the relative strength of the reflected rays and maximizes the probability of detecting the rays above the noise floor. Unfortunately, it was discovered early in the project that this criteria is never met because LRO's transmitter is intentionally turned off during these periods of time.
- The grazing event should occur over an area of the lunar south pole with low to moderate roughness.
- Multiple tracks should illuminate a similar area of the lunar surface to ensure that our measurements are repeatable.

Additional constraints to the down-selection were as follows:

a) The grazing event should occur when LRO's transmitter is turned on.

b) The grazing event should be recorded when there are no scheduling conflicts with other DSN operational tracks (since our science activity is opportunistic, our tracks were lowest in priority for DSN scheduling purposes).

c) The grazing event should ideally be recorded with a system that can measure both LRO's co-polarization and cross-polarization signals.

Given the large number of candidate options, we implemented a tool to help identify desirable surface grazing events. The tool inputs include long-term predicts of LRO's trajectory, the set of scheduled passes between LRO and White Sands, the current DSN schedule, and a roughness map of the lunar south pole. Using these inputs, the tool determines windows of opportunity that meet the down-select criteria and provides figures

of merit, such as expected sampled area or the average roughness of the terrain illuminated. Additionally, it treats constraints (a) and (b) as "hard-constraints"; i.e., if not met, the window of opportunity is immediately discarded. Alternatively, constraint (c) is considered a "soft-constraint", so the tool simply flags tracks with potential issues for further consideration.

Using this tool, a total of nine opportunities were selected and provided to the DSN scheduling team. Table 1 summarizes the timing of these tracks[2], and are identified throughout this article by the LRO orbit counter (first column). The DoY entry in the second column refers to the day-of-year in 2020. For each track, we first provide basic orbital information, including whether the spacecraft was rising or setting behind the far side of the Moon as it overflew the south pole, as well as the rise and set times for that orbit. We also provide the scheduled AOS and LOS times between LRO and White Sands, as well as the scheduling information for the Deep Space Station (DSS) that was selected to shadow the downlink. Note that the LRO operations team uses AOS and LOS to denote the times at which the White Sands antenna acquires and loses signal from LRO. Similar concepts in the DSN are known as beginning of track (BOT) and end of track (EOT), respectively. Additionally, the DSN also uses the concept of beginning and end of activity (BOA and EOA) to indicate the times at which the antenna starts and ends its pre-calibration and post-calibration processes. The amount of time elapsed for these calibration activities depends on the type of service requested and, for the purpose of our experiment, were set to 30 and 15 minutes, respectively.

Table 1. Tracks Shadowed by the DSN

Orbit	DoY	LRO			White Sands		DSN				
		Rise	Rise Time	Set Time	AOS	LOS	BOA	BOT	EOT	EOA	DSS
48161	65	Yes	5:37	6:52	5:48	6:46	5:03	5:33	5:52	6:07	26
48162	65	Yes	7:34	8:49	7:45	8:44	7:00	7:30	7:49	8:04	26
48247	72	No	4:38	5:50	5:06	5:51	5:18	5:48	5:56	6:11	26
48248	72	No	6:35	7:47	6:49	7:48	7:15	7:45	7:53	8:08	26
48249	72	No	8:32	9:45	8:47	9:45	9:12	9:42	9:50	10:05	26
48274	74	No	9:23	10:33	9:36	10:34	10:01	10:31	10:38	10:53	26
48810	118	Yes	1:29	2:40	1:35	2:33	1:00	1:30	1:45	2:00	14
48811	118	Yes	3:26	4:37	3:52	4:22	3:15	3:45	4:00	4:15	24,26
48934	128	No	2:32	3:42	2:45	3:43	3:00	3:30	3:45	4:00	26

From Table 1, the timeline of events that occurred during each experiment can be inferred, and depends on whether LRO rises or sets over the lunar limb. For convenience, the time intervals elapsed between pairs of events are reported in Tables 2 and 3, respectively (Tx ON and Tx OFF indicate the time at which LRO's transmitter was turned

[2]In this article, all timing-related information is expressed in Universal Coordinated Time (UTC). Also, unless otherwise stated, hours of the day are ante meridiem (AM).

Table 2. Timing Intervals for Tracks Where LRO Was Rising

Orbit	BOA to BOT	BOT to Tx ON	Tx On to AOS	AOS to EOT	EOT to EOA	Rise to EOT	BOT to EOT
48161	0:30	12:41	03:00	0:03	0:15	0:04	0:19
48162	0:30	12:58	03:00	0:03	0:15	0:04	0:19
48810	0:30	02:03	03:00	0:09	0:15	0:00	0:08
48811	0:30	04:23	03:00	0:07	0:15	0:18	0:15

on and off). Observe that in general all tracks were scheduled right around the expected time that LRO turned its transmitter on and off. One notable exception is the time from BOT to LRO's transmitter turning on for tracks 48161 and 48162. Since these were the first tracks attempted, we provided additional time to ensure any problems could be debugged prior to the event of interest. Another exception is the time between rise and EOT for track 48811. Unfortunately, a change in LRO's schedule resulted in an AOS time shifted from the rise time by as much as 30 minutes, causing the surface grazing event to be missed altogether. This was an unfortunate circumstance since two antennas had been scheduled for this pass.

Table 3. Timing Intervals for Tracks Where LRO Was Setting

Orbit	BOA to BOT	BOT to LOS	LOS to Tx OFF	Tx OFF to EOT	EOT to EOA	Set to EOT	BOT to EOT
48247	0:30	0:03	0:05	0:00	0:15	0:02	0:08
48248	0:30	0:03	0:05	0:00	0:15	0:02	0:08
48249	0:30	0:03	0:05	0:00	0:15	0:03	0:08
48274	0:30	0:03	0:05	0:00	0:15	0:02	0:07
48934	0:30	0:13	0:05	0:00	0:15	0:12	0:15

All tracks were scheduled well in advance to reserve time on the DSN antennas and avoid conflicts with other projects. However, tracks at the end of the 6-month experiment had to be shifted in time due to changes in LRO's orbit. Indeed, since the event of interest happens only at the lunar limbs and lasts for 10 to 15 minutes, any orbital maneuver can shift the timing of LRO's egress or ingress enough to render the previously scheduled passes useless. This eventuality occurred during the last three scheduled tracks and was corrected prior to their execution.

D. Transmitter and Receiver Specifications

1. LRO Telecom Subsystem

LRO carries a complex telecom subsystem capable of transmitting data at both S- and Ka-band (25.5 GHz) over a wide range of data rates and using different modulation and coding formats [7]. Additionally, the spacecraft carries two omnidirectional low-gain

antennas and a 75 cm diameter HGA, and was designed to transmit to either the Near Earth Network (NEN), the Space Network (SN), or the DSN. For the purposes of this work, however, only the S-band carrier sent from the spacecraft to Earth is of interest.

The characteristics of the S-band carrier depend primarily on whether the radio operated in one-way non-coherent or two-way coherent mode. For the former, the carrier frequency is derived from an onboard ultra-stable oscillator; for the latter, the transmitted frequency is proportional to the received frequency from the ground station with a turnaround ratio equal to 240/221. In either case, however, we will consider the nominal frequency of LRO's S-band downlink to be 2271.2 MHz.

Finally, LRO's high-gain antenna is designed to have a maximum gain in excess of 21 dBi using right-hand circular polarization (RHCP) at S-band. The exact radiation pattern is slightly dependent on the electrical angle of the transmitted signal [7]. However, for the purposes of this article, we will assume that it can be well approximated by the International Telecommunication Union (ITU) average radiation pattern of a point-to-point antenna [8], which is plotted in Figure 2 together with the theoretical radiation pattern of a parabolic antenna with the same diameter. Observe that there is good agreement between both models for the antenna's main lobe, but differences become notable around the nulls and at high off-axis angles. Ultimately, direct comparison with the LRO-measured radiation pattern showed better agreement with the ITU model, which justifies us choosing it over the ideal radiation pattern.[3]

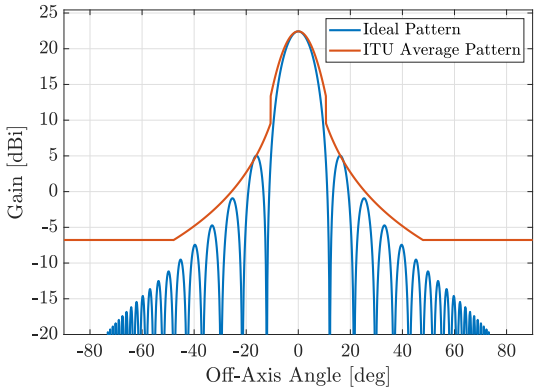

Figure 2. LRO Radiation Pattern

2. DSN Antennas

Two types of DSN antennas were used for this experiment, 34 m diameter beam waveguide (BWG) antennas and 70 m antennas. DSS-26 and DSS-24 are both BWG antennas with a 34 m parabolic dish (see reference [9] for detailed performance char-

[3]The measured radiation pattern of LRO is available in reference [7]. However, it is not provided in this article due to data restrictions.

acteristics). Unfortunately, they can only measure one polarization at S-band (this limitation only applies to 34 m BWG antennas). Therefore, dual polarization measurements can only be acquired by simultaneously scheduling two out of three 34 m antennas available at the Goldstone complex.[4] Since this is an unlikely event, most of our tracks were limited to a single 34 m antenna and thus single polarization measurements.

Alternatively, the DSN also provides a single 70 m antenna per complex. While time on these antennas is highly contended, their front-ends can provide both polarizations simultaneously, which can then be input to the DSN receiver. Ultimately, however, the choice of antenna was largely determined by the operational tracks already in the DSN schedule that constrained our experiment windows. Therefore, we scheduled most tracks with a single 34 m antenna, and were able to obtain a single track with DSS-14, the 70 m antenna at Goldstone.

3. Open-Loop Recordings

In order to capture the Doppler spread caused by scattering of the signal reflected from the lunar surface, we used the DSN's open-loop receiver, a tool used for radio science investigations, Delta-Differential Doppler (DDOR) measurements, and other DSN science activities. In open-loop reception, the electromagnetic spectrum is captured within a user-defined frequency range, down-converted via a local oscillator, and recorded to disk as digital samples [10]. This down-conversion is guided by a file of predetermined frequencies (known as tuning "predicts"), which accounts for all Doppler effects and centers the OLR samples at the expected received frequency (rather than the carrier frequency transmitted by the spacecraft). For the purposes of this experiment, the "predicts" file provided to the OLR was based on LRO's non-coherent carrier signal. Additionally, an OLR operator from our team monitored each track in real time to ensure that the LRO signal was properly recorded.

During each track, we configured the OLR to record several bandwidths, each with a different purpose. The narrowest channel, 1 kHz, was the easiest to process due to low data volume and was used primarily for quick-look analysis of the received carrier signal. Meanwhile, the 16 kHz data were wide enough to easily accommodate the frequency of the reflected signal and spreading caused by multipath effects, even if the recording predicts were tuned to the frequency of the direct carrier. Recordings at 50 and 100 kHz were also collected. While more cumbersome to work with due to increased data volume, these recordings allowed us to improve the resolution and SNR of our spectrograms, and detect the change in frequency when LRO swapped from one-way non-coherent transmit mode, to two-way coherent mode with White Sands.[5] Finally, a wideband 16 MHz

[4]The Goldstone complex also has a research and development antenna, DSS-13, available for experimental activities such as the ones performed in this work. However, limitations on the connection between DSS-13 and the OLRs at DSN signal processing center prevented us from using it. Note that these limitations are expected to be lifted in the near future.

[5]Due to the opportunistic nature of this experiment, we were not privy to the White Sands uplink

recording was also captured with reduced sampling resolution (4 bits per sample). The wideband recordings were analyzed to generate spectrograms similar to those presented in this article, but the improvement over the 100 kHz recording was not sufficiently significant to justify the additional complexity and computational time of using a larger data set.

In order to examine reflections in both co-polarization and cross-polarization signals, it was desirable to simultaneously receive RHCP and left-hand circular polarization (LHCP) whenever possible. The DSN OLRs have this capability as long as the antenna's microwave subsystem is able to route both signals to its input ports. As mentioned previously, this is not the case for 34 m BWG stations; therefore, in these cases only the LHCP was recorded.

On April 27, two attempts were made to attain both polarizations simultaneously. The first attempt was made using DSS-14, which, as previously stated, is capable of dual polarization reception at S-band. During the activity, we coordinated directly with DSN operations to confirm that the station's microwave system was configured to provide both outputs to the OLR. The second attempt, hours later, was scheduled with two antennas, DSS-24 and DSS-26, tracking at the same time, one configured for RHCP and the other for LHCP. However, due to the timing of LRO's spacecraft operations, the transmitter was turned on several minutes after the grazing opportunity and thus the signal was not available during the allotted DSN tracking time. Consequently, only the DSS-14 data are used for dual-polarization analysis in the following sections.

III. Experiment Results

In this section, we analyze the received signal for three of the nine shadowed downlinks that correspond to LRO orbits 48247, 48248, and 48810. Tracks 48247 and 48248 were executed with a 2-hour difference (i.e., after one LRO revolution around the Moon), a fact that results in LRO's orbit having minimally precessed (see Figure 3). Therefore, they cover almost the same region of the lunar surface and are good candidates to understand if the received scattering signature is correlated with lunar terrain features. On the other hand, track 48810 was conducted with DSS-14 and therefore allows us to compare the scattering signature of one site in two polarizations (RHCP and LHCP).

A. Received Signal-to-Noise Ratio and Residual Frequency

Figure 4 reports the measured power spectral density (PSD) at the carrier frequency and the residual frequency from the downlink's LHCP for consecutive tracks 48247 and 48248. Since LRO sets behind the lunar limb in these two orbits, both measurements start with LRO transmitting in two-way coherent mode from White Sands. Two to

---

profile. Therefore, after LRO started transmitting in two-way non-coherent mode, our uploaded predicts to the OLR had an offset of 30 kHz in the worst case.

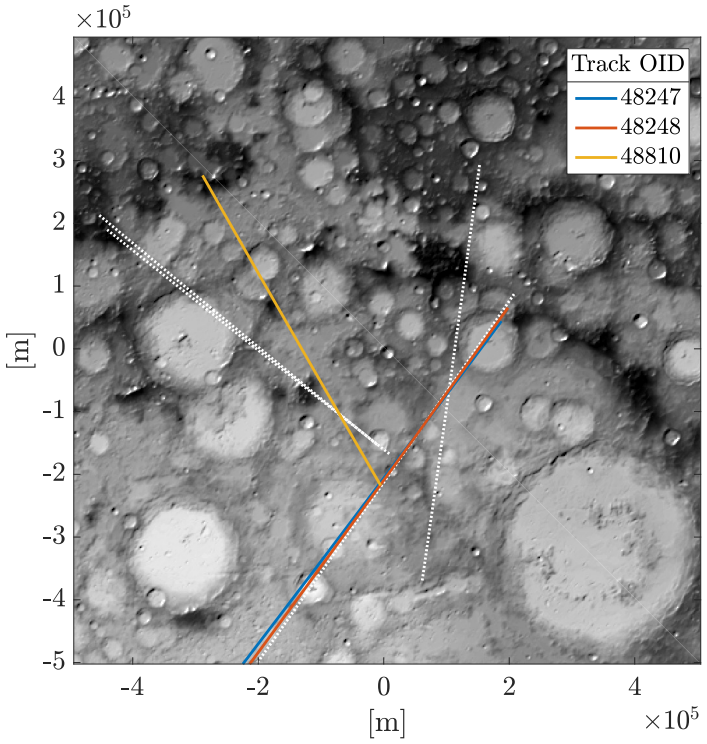

Figure 3. LRO Ground Tracks. White lines represent tracks for which OLR samples were recorded and analyzed, but results are not included in this section.

three minutes into the recording, White Sands stops uplinking and the received signal experiences a sudden jump in frequency (LOS for tracks 48247 and 48248 was scheduled at 05:51 and 07:48, respectively, which matches our measurements within a few seconds). After that event, LRO is transmitting a one-way non-coherent downlink carrier generated using its internal oscillator. Furthermore, we can see that the residual frequency becomes approximately zero, which indicates that the OLR was properly configured to receive this one-way carrier.

Figure 5 provides the same information from track 48810 for both the RHCP and LHCP. In this case, the sequence of events is inverted since LRO rose over the lunar limb. Therefore, we initially have no signal present as LRO's transmitter is not turned on yet, followed by a period of time with close-to-zero frequency residuals, which corresponds to transmission of the one-way carrier. Next, there is a period of time exhibiting large fluctuations in signal power. This period starts with White Sands AOS, which is scheduled to occur at 01:35, and lasts for about 1 minute, the time it takes for LRO's radio to fully acquire the uplink carrier. From that point on, LRO transmits a stable two-way coherent carrier with more than 20 dB of SNR in the RHCP. The LHCP, on the other hand, has its SNR reduced by approximately 5 dB, but the recording still shows a signal several dB higher than noise floor.

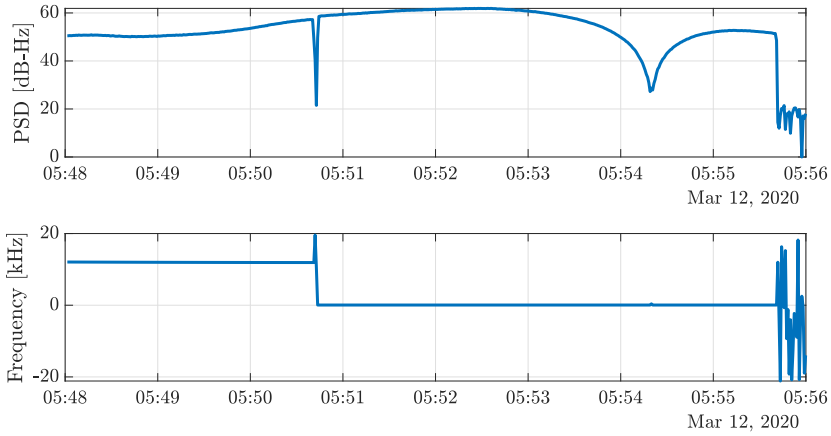

(a) Track 48247 (LHCP)

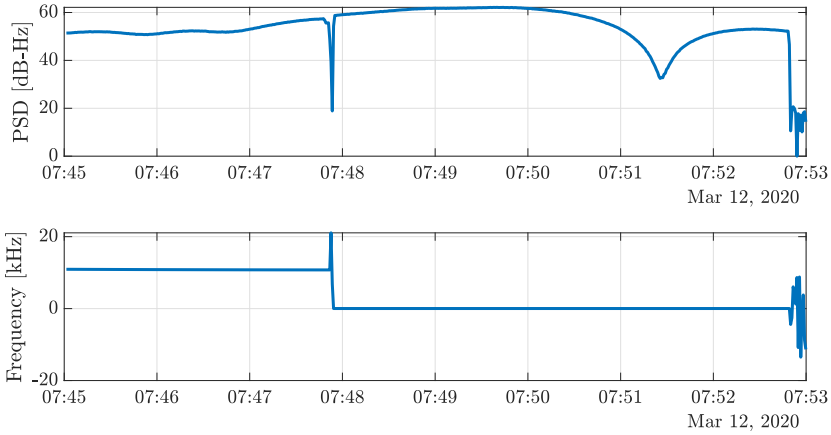

(b) Track 48248 (LHCP)

Figure 4. Received PSD and Residual Frequency

B. Scattering Signatures

We now focus our attention on detecting reflections from the lunar surface in the recorded signals. To do so, we compute the spectrogram of the received signal using 100 kHz OLR recordings with a frequency resolution of 30 Hz. Note that since the reflection area on the surface of the Moon is not co-located with the spacecraft, the Doppler shift experienced by the reflected rays should not be centered around the received carrier frequency, thus facilitating their detection on the spectrogram.

Figure 6 shows the calculated spectrograms for both tracks 48247 and 48248. Once again, there is a clear jump in frequency at around 3 minutes into the recording when the carrier switches from coherent to non-coherent mode. More importantly, there are scattered components close to the carrier for the majority of the recording (at $t >$ 400 seconds, LRO is already in front of the Moon, which explains why the scattered

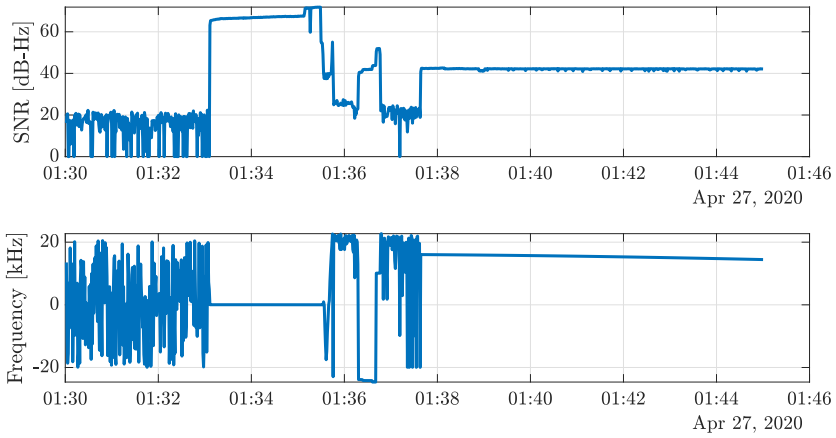

(a) Track 48810 (RHCP)

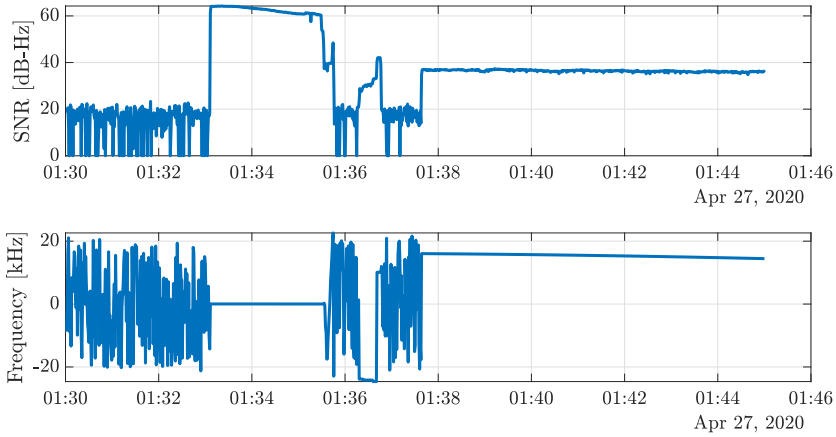

(b) Track 48810 (LHCP)

Figure 5. Received SNR and Residual Frequency

components cease). These scattered components are heavily attenuated and do not have a significant impact on the link performance, but can nonetheless be discerned above the noise floor.[6]

To facilitate the rest of the analysis, we will concentrate on the portion of the recording where LRO transmitted a non-coherent carrier. Figure 7 shows the spectrograms for the four passes of interest. It can be clearly observed that the scattering signature of tracks 48247 and 48248 is very similar due to the fact that the same area of the lunar surface was being sampled. On the other hand, the scattering signature of track 48810 is significantly different in the RHCP and LHCP, a fact that we are currently investigating and hope exploit by correlating the CPR with terrain roughness maps.

[6]During the two-way coherent portion of the spectrogram we also detect tones transmitted at frequencies equidistant from the main carrier. These are considered spurious tones and therefore not related to any multipath effects.

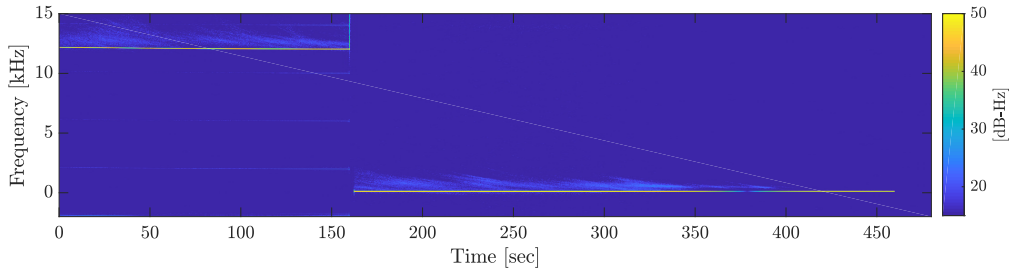

(a) Track 48247

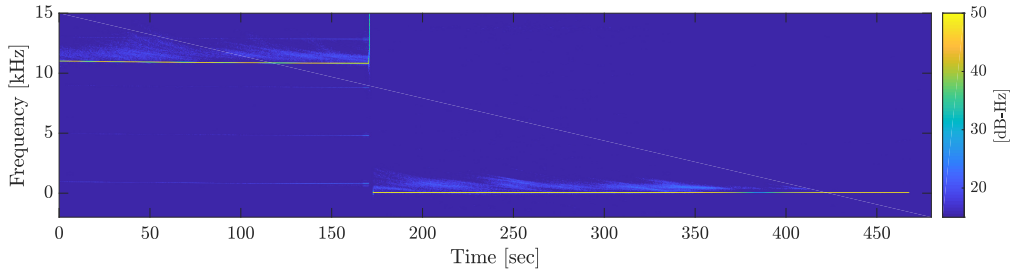

(b) Track 48248

Figure 6. Spectrograms for Tracks 48247 and 48248

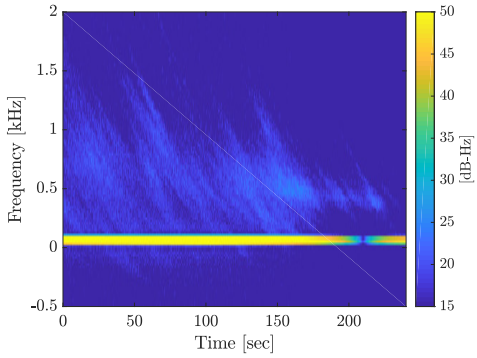

(a) Track 48247 (LHCP)

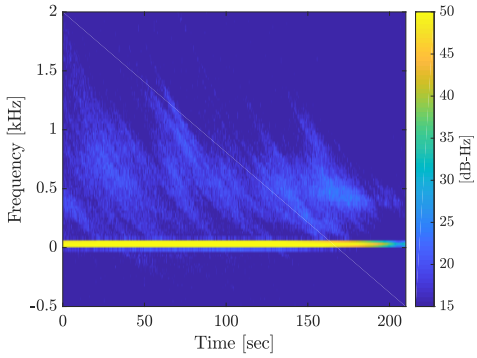

(b) Track 48248 (LHCP)

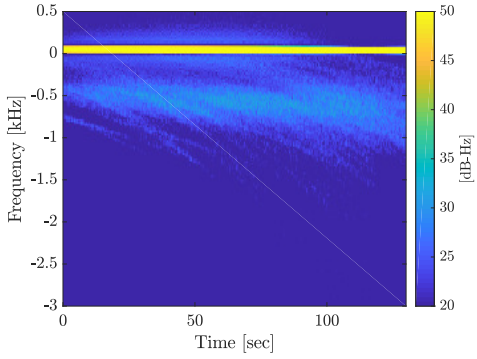

(c) Track 48810 (RHCP)

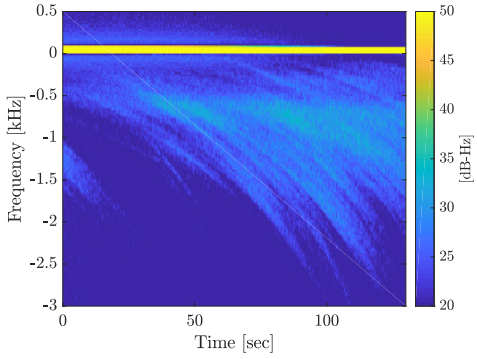

(d) Track 48810 (LHCP)

Figure 7. Spectrograms for Tracks 48247 and 48248

Figure 7 also motivates several additional remarks. First, the Doppler shift experienced by the reflected rays is skewed from the carrier either positively (tracks 48247 and 48248) or negatively (tracks 48810). This is due to the fact that tracks 48247 and 48248 occurred while LRO was setting behind the lunar limb, while track 48810 captured an instance of LRO egressing lunar occultation. Additionally, the spread of received scattered frequencies also varies. For tracks 48247 and 48248, most signal components are located at $f \in [0, 1]$ kHz. In contrast, the LHCP of track 48810 has reflected rays shifted by as much as 3 kHz.

C. Specular Reflection Point

Up until this point, we have limited ourselves to analyzing the received samples without contextual information on where LRO was located at the time of the scattering event. We now expand the analysis by correlating the measurements with reconstructed LRO trajectories and high-resolution digital elevation maps (DEM) from the Lunar Orbiter Laser Altimeter (LOLA) instrument, also onboard LRO. Furthermore, while such analysis can be performed over the entire pass, we typically only report results for a given instant in time. This instant of time is somewhat arbitrarily selected, but must have a strong scattered component.

The specular reflection point is defined as the point on the reflecting surface where the angle of arrival (also known as incidence angle and denoted by θ in Figure 1) and angle of departure of an incident and reflected ray are equal. In a three-dimensional system, an additional constraint must be imposed, namely that the incident and reflected rays be contained in a single plane. In other words, using the angles specified in Figure 8, the specular point is defined as the coordinate on the lunar surface where $\theta_i = \theta_r$ and $\gamma_i = \gamma_r$.

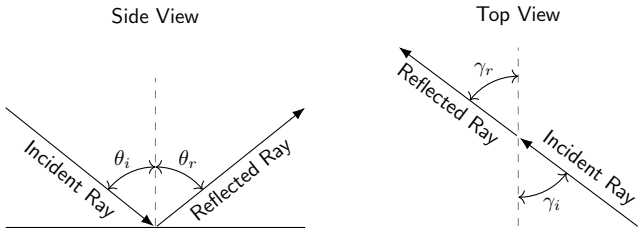

Figure 8. Specular Point Geometry

To estimate the location of the specular point at any point in time, we first take surface altitude measurements in a stereographically projected lunar DEM and transform them to three-dimensional cartesian coordinates in a Moon-fixed reference frame. We then use the LRO trajectory to estimate a set of vectors that originate at LRO and intersect with all pixels in the DEM. Similarly, we use the trajectory information of the DSN stations to estimate a set of vectors that originate at every pixel of the same DEM and

arrive at DSS-26.[7] Next, we estimate the normal to the lunar surface at each pixel in the DEM, assuming the Moon is perfectly spherical and use that information, together with the previous vectors, to estimate θ_i, θ_r, γ_i, and γ_r. Finally, we compute the overall error angle for any given pixel as

$$\epsilon = \sqrt{(\theta_i - \theta_r)^2 + (\gamma_i - \gamma_r)^2}, \tag{1}$$

and associate the specular reflection with the pixel of minimal ϵ.

Figure 9 plots the calculated error angle ϵ superimposed with the lunar surface DEM. The red dashed line plots LRO's orbit for the duration of the track, while the blue line points towards DSS-26 and the green dot indicates the position of the specular reflection. Observe that ϵ correctly aligns specular reflection point, LRO and DSS-26 in a plane.

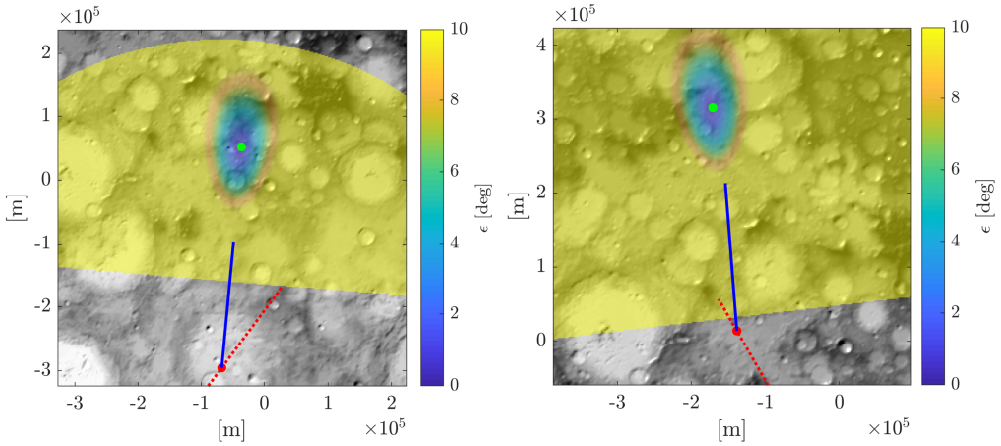

(a) Track 48247 **(b) Track 48810**

Figure 9. Angular Maps for Tracks 48247 and 48810

D. Doppler Shift of the Scattered Signal

We now focus our attention on the Doppler shift experienced by rays reflected off of the lunar surface. From reference [11], we know that in a Moon-fixed reference frame, the Doppler shift experienced by a reflection from the lunar surface can be computed as

$$f_d = -\frac{\vec{v}_1 \cdot \vec{u}_1 + \vec{v}_2 \cdot \vec{u}_2}{c + \vec{v}_2 \cdot \vec{u}_2} f_c, \tag{2}$$

[7] DSS-26, DSS-24, and DSS-14 are close enough in latitude/longitude that the error induced by computing the specular point using a single station is negligible.

where

$$\vec{v_1} = -\vec{v}_{LRO}, \tag{3}$$

$$\vec{v_2} = \vec{v}_{DSS}, \tag{4}$$

$$\vec{u_1} = \frac{\vec{p}_{px} - \vec{p}_{LRO}}{\|\vec{p}_{px} - \vec{p}_{LRO}\|}, \tag{5}$$

$$\vec{u_2} = \frac{\vec{p}_{DSS} - \vec{p}_{px}}{\|\vec{p}_{DSS} - \vec{p}_{px}\|}, \tag{6}$$

c denotes the speed of light in the vacuum; f_c denotes the carrier frequency transmitted by LRO; $\vec{p}_{px}$, $\vec{p}_{LRO}$, and $\vec{p}_{DSS}$ denote the position of a DEM pixel, LRO, and DSS-26; and $\vec{v}_{LRO}$ and $\vec{v}_{DSS}$ denote the velocity of LRO and DSS-26. Note that because we have chosen to perform the calculation in a Moon-fixed reference frame, the velocity of any point on the lunar surface is by definition zero. Note also that Equation (2) returns the Doppler shift in the instant of time where an incident ray hits the surface of the Moon. Therefore, a time correction of

$$t = t' + \frac{r(t')}{c} \tag{7}$$

needs to be applied to recover the instant of time at which a given Doppler shift will be received at the DSN station. In this notation, t indicates instants of time referenced to the Earth ground station, t' denotes the associated instant in time at the lunar surface, and $r(t')$ is the distance between a given pixel on the lunar surface and DSS-26. In other words, Equation (7) describes the shift in time of the Doppler shift measurements by the propagation delay between the Earth and the Moon.

Figure 10 shows the result of the calculation for all points on the lunar surface visible from LRO at two arbitrary instants of time of tracks 48247 and 48810. Observe that in both cases, the specular point lies in the transition region between Doppler shifts exceeding ±2 kHz, consistent with the scattering signatures from Figure 7, where most

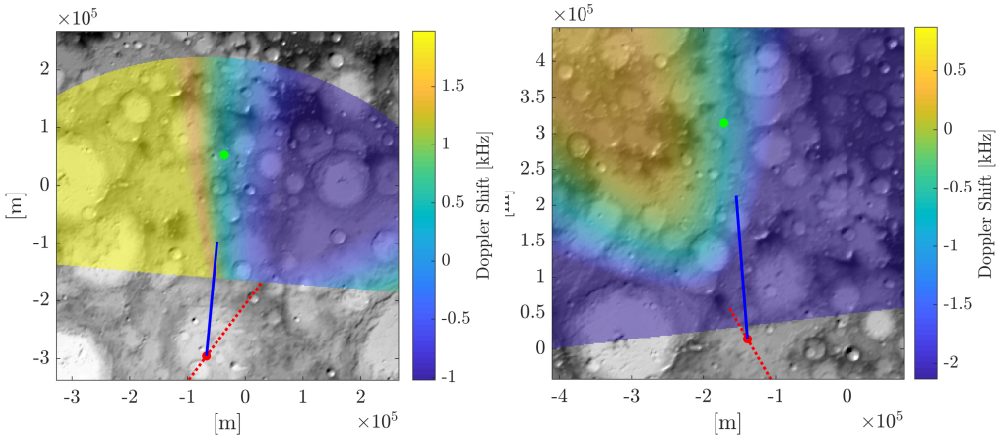

(a) Track 48247 **(b) Track 48810**

Figure 10. Doppler Shift for Tracks 48247 and 48810

of the scattering power lies within 2 kHz from the received carrier. This suggests that the spread of the scattered components in Figure 7 can be used to bound the scattering region, a technique that is further discussed in Section III.F.

Finally, Figure 11 plots the predicted Doppler shift of the specular reflection over time for tracks 48247 and 48810. Results indicate an almost perfect agreement between our estimates and the measured scattered signal, especially for the RHCP of track 48810.

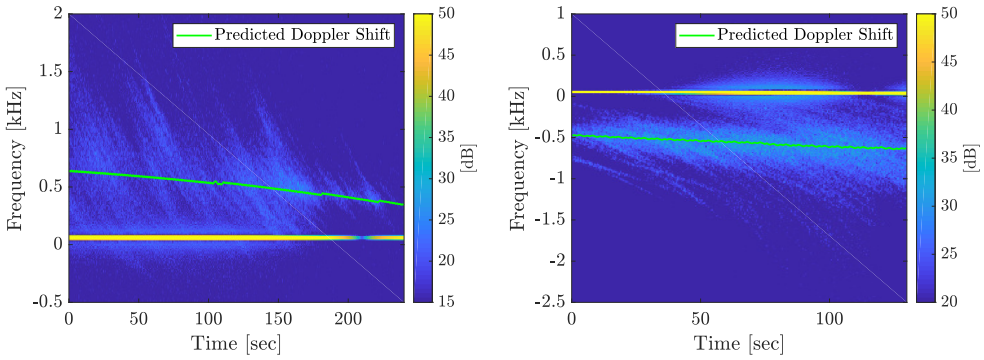

(a) Track 48247 **(b) Track 48810 (RHCP)**

Figure 11. Relative Fresnel Index for Tracks 48247 and 48810

E. Fresnel Zones

The relative Fresnel index is another well-known figure of merit that is typically considered in remote sensing experiments (see reference [12], for instance). The relative Fresnel index indicates the Fresnel zone that includes a given reflection point and provides an indirect measure of the difference in propagation delay between the scattered and line-of-sight (LoS) rays.

Formally, the n-th Fresnel zone is defined as the locus of points where a reflection ray experiences a phase shift equal to $n\frac{\lambda_c}{2}$ when compared with the direct LoS ray. This locus of points can be shown to be an ellipsoid in three dimensions, with foci located at the transmitter and receiver, respectively. Using the notation from Figure 12, the n-th Fresnel zone is defined as the set of points P such that

$$d_1 + d_2 - d = n\frac{\lambda_c}{2}, \tag{8}$$

where λ_c is the carrier frequency and, in our case, d_1 is the distance from LRO to the lunar surface, and d_2 is the distance between the lunar surface and a DSN station. Furthermore, and assuming that the speed of light is approximately the same in the vacuum and in Earth's atmosphere, we can rewrite Equation (8) in terms of propagation delay as follows:

$$\tau_1 + \tau_2 - \tau = \frac{n}{2f_c}, \tag{9}$$

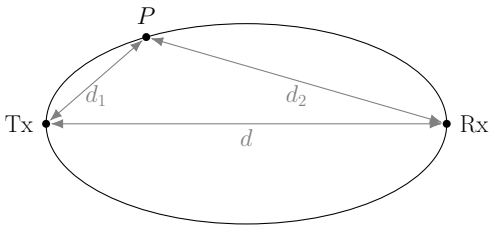

Figure 12. Fresnel Zone Geometry

or, equivalently,

$$n = 2f_c\Delta\tau, \tag{10}$$

where $\Delta\tau$ is the difference in propagation delay experienced by the ray that bounced off of the lunar surface and the direct LoS ray. Therefore, we have concluded that the Fresnel index can be used as an indirect measure for the delay spread of the reflected rays.

Finally, it is sometimes convenient to define the relative Fresnel index with respect to the specular reflection point: $\eta = n - n_s$, where n_s is the Fresnel index of the specular point. Simple algebraic manipulation yields

$$\eta = 2f_c\delta\tau, \tag{11}$$

where $\delta\tau = \sum_{\forall i} \tau_i - \tau_{i,s}$ represents the total difference in propagation delay between the specular ray and an arbitrary reflected ray. This figure of merit is plotted in Figure 13 for all pixels of the lunar surface that are in view of LRO and DSS-26 at an arbitrary point in time. It can be observed that lines of constant relative Fresnel index are shaped like ellipses on the lunar surface, which is consistent with results reported in reference [13] for bistatic ranging over a spherical surface.

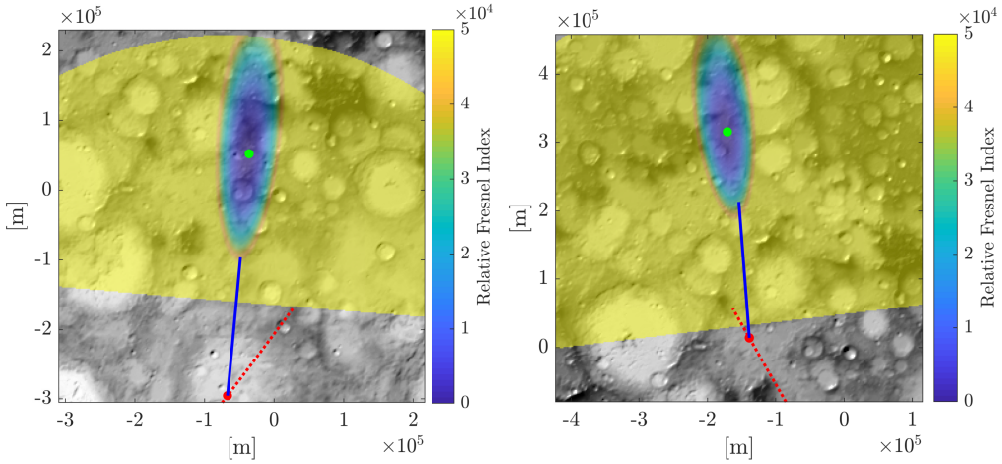

(a) Track 48247 **(b) Track 48810**

Figure 13. Relative Fresnel Index for Tracks 48247 and 48810

F. Scattering Area

The results from Sections III.D and III.E can now be combined to quantify the scattering area of the reflected signal. This is typically achieved by calculating iso-Doppler and iso-delay lines, which partition the scattering area in regions of constant Doppler and delay. These partitions, in turn, can be used to associate heterogeneous physical properties to different parts of the scattering area without having to sample the areas individually, a technique that is well-known in remote sensing applications (c.f. [12]).

In order to fully take advantage of the iso-Doppler and iso-delat analysis of the scattering area, measurements of both the Doppler and delay properties of the received signal are needed. This requires the transmitter to send a signal with both good temporal and spectral resolution, such as pseudo-noise (PN) sequence sounders (including Global Navigation Satellite System signals), chirp sounders, and trains of linearly modulated waverforms, among others [14]. Unfortunately, LRO only transmits a single tone at the carrier frequency as it overflies the limbs of the Moon. Therefore, our measurements have excellent spectral resolution, but poor temporal properties, which in turn limits our ability to properly constrain the scattering area.

Figure 14 plots the iso-delay and iso-Doppler lines over the scattering area at a given point in time during tracks 48247 and 48810. These isometric lines are overlaid on a color-coded map that indicates the relative strength of a ray that departs LRO's HGA and is reflected off of a pixel on the surface DEM. It can be observed that the width of the resulting ellipse will be directly related to the Doppler spread of the received signal, thus allowing us to bound its extent in this direction. Similarly, the relative gain between different pixels also constrains the scattering area. Indeed, if the difference is large enough, then the signal power of the reflected ray will fall below the noise floor and will therefore not be detectable. On the other hand, since we have no delay

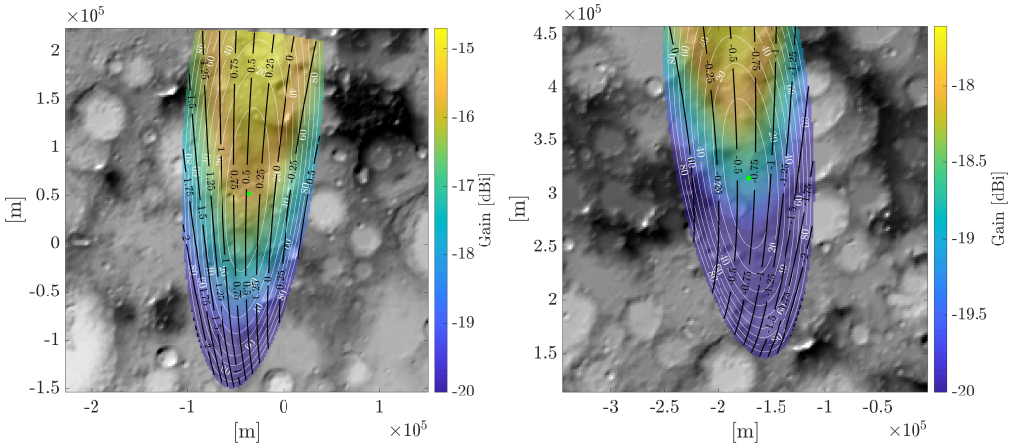

(a) Track 48247 (b) Track 48810

Figure 14. Iso-Doppler (black) and Iso-Range (white) Lines for Tracks 48247 and 48810. Iso-Doppler lines report Doppler shift from the carrier, in kHz. Iso-range lines report the relative Fresnel index scaled by a factor of 1000.

information in the collected samples, there is no way for us to delimit the Fresnel zone index. Therefore, our estimated scattering area will always resemble an ellipsoid, as seen in Figure 14.

IV. Conclusions

This article is the first of a two-part series where we report the results of an experimental campaign conducted during the first half of 2020. The goal of this campaign was to record multipath reflections from the lunar south pole using LRO's S-band downlink carrier, and analyze the scattering signature to understand the resulting Doppler spread and the characteristics of the reflection terrain that caused the spread. All experiments were conducted opportunistically, i.e., without any operational impact to the mission, and required simply shadowing downlink passes between LRO and its primary ground station from a closely co-located DSN station. While the opportunistic nature of the experiment expedited its completion, it also resulted in limited science output since LRO's downlink signal and orbit were not designed for this activity.

The main focus of this article is to provide a detailed description of how the experiment was planned and executed, as well as an introductory overview of the samples collected and how they can be analyzed for science purposes. Our results show that multipath reflections off of the lunar south pole were collected in all but one of the one passes, regardless of whether the spacecraft was rising over or setting behing the far side of the Moon. We also showed that we can use reconstructed spacecraft trajectories to pinpoint the specular point of reflection and match its calculated Doppler shift to what is measured from the recorded samples. Finally, we show that while the lack of temporal resolution in LRO's carrier limits our ability to properly determine the scattering area, we can still estimate it assuming an ellipsoidal shape and use it to correlate the Doppler spread with the terrain roughness.

Finally, the successful completion of this experiment serves as a proof of concept for similar activities with upcoming lunar spacecraft. For instance, the Korea Pathfinder Lunar Orbiter (KPLO) will provide an opportunity to collect similar measurements at both S- and X-band. Similarly, secondary payloads in the Artemis-1 mission, such as the Lunar IceCube and the Lunar H-Map, are also good candidates and might allow us to perform targeted observations where the downlink signal is not just a single carrier tone.

Acknowledgments

We would like to thank Jack Lippincott of the Deep Space Network, Ralph Casasanta of LRO Ground System and Operations Support, George Martinez of JPL (Network Operations Project Engineer), Steve Slojkowski (Flight Dynamics Facility Lead) of OMITRON, GSFC, Rick Saylor of NASA GSFC, and Harvey W. Elliott of NASA GSFC for their help and contributions while planning and executing this experiment.

References

[1] S. Nozette, C. Lichtenberg, P. Spudis, R. Bonner, W. Ort, E. Malaret, M. Robinson, and E. Shoemaker, "The Clementine Bistatic Radar Experiment," *Science*, vol. 274, no. 5292, pp. 1495–1498, 1996.

[2] N. Stacy, D. Campbell, and P. Ford, "Arecibo Radar Mapping of the Lunar Poles: A Search for Ice Deposits," *Science*, vol. 276, no. 5318, pp. 1527–1530, 1997.

[3] D. B. Campbell, B. A. Campbell, L. M. Carter, J.-L. Margot, and N. J. Stacy, "No evidence for thick deposits of ice at the lunar south pole," *Nature*, vol. 443, no. 7113, pp. 835–837, 2006.

[4] J. Honeycutt. NASA'S Space Launch System: Enabling ARTEMIS and Transformative Science Missions. NASA. https://www.nationalacademies.org

[5] M. Sanchez Net, "Analysis of the Fading Channel in Downlinks from the Lunar South Pole to the Deep Space Network," *The Interplanetary Network Progress Report*, vol. 42-216, Jet Propulsion Laboratory, Pasadena, CA, pp. 1–30, February 2019. https://ipnpr.jpl.nasa.gov/progress_report/42-216/42-216C.pdf

[6] Siekerski, Jim, et al., "X-band Comm System Preliminary Design Assessment," NASA, Tech. Rep., June 2020.

[7] Goddard Space Flight Center, "Radio Frequency Interface Control Document Between Lunar Reconnaissance Orbiter and the Near Earth Network, Deep Space Network and Space Network," NASA, Tech. Rep. 450-RFICD-LRO/NEN/DSN/SN, February 2009.

[8] International Telecommunications Union, "Mathematical model of average and related radiation patterns for line-of-sight point-to-point radio-relay system antennas for use in certain coordination studies and interference assessment in the frequency range from 1 GHz to about 70 GHz," International Telecommunications Union, Tech. Rep. F.1245-3, January 2019.

[9] Jet Propulsion Laboratory, "34-m BWG Stations Telecommunication Interfaces," Jet Propulsion Laboratory, Tech. Rep. 810-005, 104, Rev. L, August 2019.

[10] S. W. Asmar et al., "Cassini Radio Science User's Guide," Jet Propulsion Laboratory, Tech. Rep. Version 1.1, September 2018. https://pds-rings.seti.org/cassini/rss/Cassini%20Radio%20Science%20Users%20Guide%20-%2030%20Sep%202018.pdf

[11] Goddard Space Flight Center, "The Doppler Equation in Range and Range Rate Measurements," NASA, Tech. Rep. X-507-65-385, October 1965. https://ntrs.nasa.gov/archive/nasa/casi.ntrs.nasa.gov/19660010159.pdf

[12] Y. Jia and Y. Pei, "Remote sensing in land applications by using gnss-reflectometry," in *Recent Advances and Applications in Remote Sensing.* IntechOpen, 2018.

[13] M. S. Haynes, "Surface and subsurface radar equations for radar sounders," *Annals of Glaciology*, pp. 1–8, 2020.

[14] G. Matz and F. Hlawatsch, "Fundamentals of time-varying communication channels," in *Wireless Communications over Rapidly Time-Varying Channels.* Elsevier, 2011, pp. 1–63.